DOTA	1,4,7,10-Tetraazacyclododecane-1,4,7,10-tetraacetic acid
EDC	1-ethyl-3-(3-dimethylaminopropyl) carbodiimide hydrochloride
EPR effect	enhanced permeability and retention effect
GPC	gel permeation chromatography
ICP	inductive coupled plasma
MRI	magnetic resonance imaging
MWCO	molecular weight cut-off
PEG-P(Lys)	poly(ethylene glycol)-b-poly(L-lysine)
ROI	region of interest
TGF-β	transforming growth factor β
TR/TE	repetition time/echo time

INTRODUCTION

Nowadays, targeting potential anticancer drugs to solid tumors by means of nanocarriers is a promising tool to maximize anticancer activity. This entire strategy for tumor targeting is based on the enhanced permeability and retention (EPR) effect (1,2). It is a well-known phenomenon that solid tumors have leaky blood vessels, namely, macromolecules of more than 40 kDa show substantial extravasation from the leaky tumor blood vessels, resulting in a large amount of accumulation in solid tumors. Many researchers have focused on macromolecular drugs that have sizes in the nanometer region to develop selective tumor targeting through the EPR effect (3). Improvement of pharmacokinetics of poorly soluble anticancer drug by means of such nano-sized drug carriers achieved long-circulation of the drug in blood which is necessary for selective tumor targeting through the EPR effect. This selective drug targeting leads to improved chemotherapy of the anticancer drug and diminishes negative side effects.

A doxorubicin encapsulated in liposome covered with poly(ethylene glycol) on the surface was approved as Doxil for treatment of Kaposi sarcoma (4). Polymer therapeutics, such as polymer-drug conjugate and polymeric micelle carriers, have been developed (5,6).

However, in our recent study on transparent chambers and a vital microscopic systems, we obtained some additional knowledge about EPR-based targeting system (7). That study examined the permeability of FITC-labeled polymeric micelles at different tumor growth stages relative to Yoshida ascites sarcoma in LY80. The FITC-labeled polymeric micelle was distributed in vessels at the interface between normal and tumor tissues, and the interface between tumor tissues and necrotic areas. It was found that the polymeric micelle accumulated in necrotic areas with dysfunction of the circulatory system. The study showed that the polymeric micelle was not accumulated in 1 mm of the microtumor without necrotic areas. This observation indicates that the tumor blood vessels in microtumors did not leak nanocarriers as compared with the advanced tumor model for common antitumor activity experiments.

Combretastatin A-4 is known as an anticancer drug that acts to tubulin by disrupting tumor vessels (8–18). One of the combretastatin A4 derivatives, Cderiv, was developed by Hatanaka *et al.* and Ohsumi *et al.* in 1998 (Fig. 1a) (10,11). Cderiv also exhibited a powerful vascular disrupting effect by intraveneous injection (8–10). The vascular disrupting effect is induced by strong interruption of tumor blood flow, which prevents nutrient supply to solid tumors and leads to necrosis in tumors (15–18). Recently, our research showed that Cderiv changed microenvironments of microtumors so that the new environments were similar to the environments characteristic of advanced tumors (19). Namely, the treatment of Cderiv induced the EPR effect in 1 mm of microtumors. A detailed whole mechanism of combretastatin A-4 derivatives including Cderiv is not completely understood yet; however, morphological and functional alternations have been seen in endothelial cells (15). Most likely, Cderiv acts indirectly in contractile arterioles of tumors, rather than directly on tumor vessels. This Cderiv pretreatment would be a new methodology to enhance EPR-effect-based delivery of therapeutic agents, as well as diagnostic agents.

Evaluation of pharmacokinetics, biodistribution, and especially drug delivery efficiency by non-invasive imaging techniques has recently become more important (20–22). Of several modalities, such as PET, CT, and MRI, MRI is a non-invasive method for three-dimensional images with high spatial resolution. Paramagnetic gadolinium chelates, such as gadolinium(III) chelates, are often used as MRI contrast agents to enhance the signal in target tissues where the contrast agents are localized (23).

A previous report on a polymeric micelle MRI contrast agent showed passive accumulation in a solid tumor, resulting in intensive enhancement of T_1-weighted signals in the tumor tissues (24). This MRI contrast agent exhibited similar pharmacokinetics as compared to a polymeric micelle anticancer drug carrier, adriamycin-encapsulating polymeric micelle (ADR-micelle) (25,26). Their structures are shown in Fig. 1b and c. As well as the pharmacokinetics, biodistribution including tumor accumulation of the MRI contrast agent was similar to that of the ADR-micelle. For example, 24.6% and 22.5% of injected dose of the ADR-micelle and the polymeric micelle MRI contrast agent were found in blood at 24 h after intravenous injection, respectively. Accumulations in C26 tumor tissues were 9.6%ID/g and 6.1%ID/g at 24 h for the ADR-micelle and the contrast agent, respectively. These results indicated that the tumor diagnosis by means of the polymeric micelle MRI contrast agent can help to predict the targeting efficiency

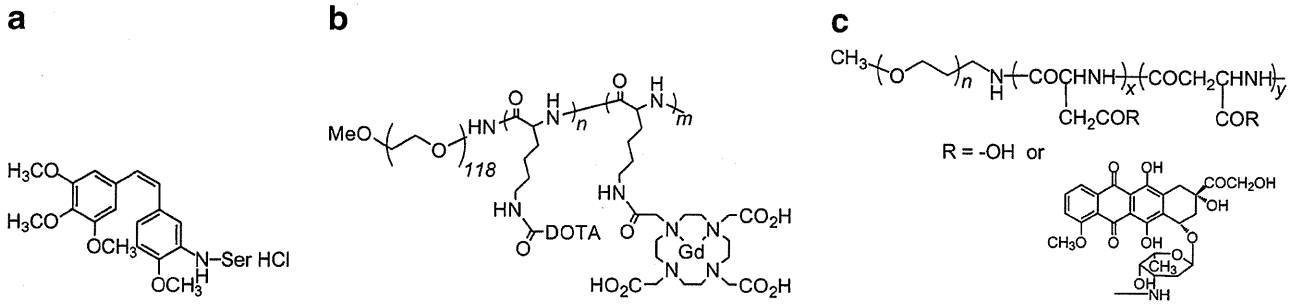

Fig. 1 Structure of (**a**) Cderiv, (**b**) polymeric micelle MRI contrast agent, and (**c**) ADR-micelle.

of the anticancer-drug-encapsulating polymeric micelle, such as the ADR-micelle.

The combination of a therapeutic drug and a diagnostic contrast agent incorporated in the same carrier system can be considered effective in the evaluation of therapeutic efficacy. This system would be a great potential for improvement of therapeutic efficacy, called as "theragnosis."

Cderiv was used to enhance permeability for improvement of the tumor targeting efficiency of a polymeric micelle carrier system. We evaluate in the present study whether Cderiv pretreatment enhances the tumor targeting of the polymeric micelle MRI contrast agent and the adriamycin-encapsulated polymeric micelle. The current study performed an MRI to evaluate the signal intensities in the tumor area. Antitumor activity was studied when this combination of the Cderiv pretreatment with ADR-micelles was used on 44As3-bearing mice (27).

MATERIALS AND METHODS

Preparation of Polymeric Micelle MRI Contrast Agents

Preparation of a polymeric micelle MRI contrast agent was reported previously (24). Briefly, a polymerization of Lys(Z) *N*-carboxy anhydride from PEG-NH_2 (Mw = 5,200) gave a poly(ethylene glycol)-b-poly[ε-(benzyloxycarbonyl)-L-lysine] (PEG-P(Lys(Z)). PEG-P(Lys(Z)) was dissolved in trifluoroacetic acid. Anisole and methanesulfonic acid were added to the solution. The mixture was stirred for 1 h to hydrolyze the protecting group. The solution was diluted with distilled water, then the excess of acid was extracted with diethylether until an organic layer became neutral. The obtained aqueous layer was neutralized by an addition of triethylamine, and dialyzed against 0.02 N NaOH and distilled water against SpectraPor 6 (MWCO = 1 k) membrane. Lyophilization gave white powder of PEG-P(Lys).

The obtained a poly(ethylene glycol)-b-poly(L-lysine) (PEG-P(Lys)) was a fully conjugated using mono *N*-hydroxysuccinimide ester of 1,4,7,10-Tetraazacyclododecane- 1,4,7,10-tetraacetic acid (DOTA) (1.3 eq *vs* lysine residues) and triethylamine in dried DMF. The reaction mixture was stirred overnight at 50°C. The resulting mixture was first dialyzed against 0.02 N HCl and then against distilled H_2O 5 times. The obtained polymer was dissolved in H_2O at a polymer concentration higher than 15 mg/mL and dialyzed against H_2O 3 times. Lyophilization gave poly(ethylene glycol)-*b*-poly(L-lysine-DOTA) (PEG-P(Lys-DOTA)) as white powder.

The conjugation was confirmed by ^{1}H-NMR under an alkali condition (pH > 10 in D_2O). The conjugated number of DOTA moiety was calculated from peak ratio between CH_2 protons of PEG at 3.73 ppm and 26H of DOTA and lysine protons in the range between 3.36 and 2.18 ppm.

The DOTA-conjugated block copolymer, PEG-P(Lys-DOTA), was mixed with $GdCl_3 \cdot 6H_2O$ at 50°C for 3 h in the range of pH 6–6.5. After several dialyses against water, Gadolinium-chelated PEG-P(Lys-DOTA-Gd) was obtained. ICP (SPS7800, SII Nano Technology Inc., Tokyo, Japan) was used for the determination of gadolinium content in the polymer. This block copolymer formed a polymeric micelle in an aqueous solution, and we detected the formation of polymeric micelle by DLS and GPC analysis.

Preparation of Adriamycin-Encapsulated Polymeric Micelles (ADR-micelles)

An adriamycin (ADR)-encapsulated polymeric micelle (ADR-micelle) was prepared according to a previously reported procedure (24,25). First, a block copolymer, poly (ethylene glycol)-*b*-poly(aspartic acid) (PEG-P(Asp)) (PEG_{Mw} = 12,000, Asp unit = 19), was synthesized from poly(ethylene glycol)-*b*-poly(β-benzyl L-aspartate). ADR was chemically conjugated to the aspartic acid of the block copolymer by EDC-mediated coupling reaction (63% conjugation to Asp unit). Then, free ADR was physically encapsulated in the block copolymer, which formed a polymeric micelle. ADR·HCl was dissolved in DMF with 1.3 equivalents of triethylemiane (*vs* ADR·HCl), and the ADR solution was mixed with the chemically ADR-

conjugated PEG-P(Asp-ADR). The mixture was stirred for 2 h at room temperature. The mixture was dialyzed with SpectraPor6 membrane against distilled water. The obtained solution was concentrated by polyethersulfone ultrafiltration membrane (MWCO = 100 k) equipped with an ultrafiltration unit (Amicon, Stirred Ultra Filter Cell). Physically encapsulated ADR was determined by an HPLC system (LC-2000 series, Jasco, Tokyo, Japan) equipped with a μBondasphere (Waters, Tokyo, Japan) column in acetonitrile/H_2O (including 1% of acetic acid) as an eluent. ADR was detected by measuring the absorbance at 485 nm. The conjugated ADR was worked only for stable encapsulation of free ADR, and no release of free ADR from the conjugate was found (28). We discussed only the physically encapsulated ADR for the determination.

MRI Study of Colon 26 CDF_1 Mice

Isoflurane (1.0–1.5%) was used for anesthesia in the MRI study. CDF_1 female mice bearing a colon 26 tumor ($n=4$) were intravenously injected with Cderiv (Tokyo Kasei Kogyo Co.) at a dose of 20 mg/kg. The size of the tumors was 50–150 mm^3. Either 72 h or 24 h from the Cderiv pretreatment, polymeric micelle MRI contrast agent was injected at a dose of 0.05 mmol Gd/kg into a mice tail vein.

MR images were taken with a Varian NMR system at 9.4T magnetic field. We performed a T_2-weighted fast spin echo (TR = 2,500 ms, ETL = 8, ESP = 4, effective TE = 48) and a T_1-weighted gradient echo (TR/TE = 8.0/4.2, flip angle = 30°, field of view of 50 × 30 mm, a matrix size of 192 × 192, and 2 mm for coronal thickness, and TR/TE = 8.0/4.5, flip angle = 30°, field of view of 45 × 45 mm, a matrix size of 192 × 192, and 2 mm for axial thickness). The signal intensity of the ROI was compared with the intensity of a stock solution of 0.1 mM gadolinium ion in agarose gel. For quantitative determination of gadolinium content in colon 26 tumor, the tumor samples were dissolved in the acid mixture of 98% H_2SO_4 and 62% HNO_3, and oxoammonium salt (1:2:1, v:v:v), and then were determined by means of ICP. For normalized signal intensity relative to the T_1-weighted images, the tumor area was selected as a ROI. The signal intensity of the ROI was compared with the intensity of a stock solution of 0.1 mM gadolinium ion in agarose gel. The relative signal intensity of the ROI at 24 h after the MRI contrast agent injection was compared to the signal intensity before the injection.

In Vivo Antitumor Activity

Antitumor activity against solid tumors was evaluated in human gastric scirrhous carcinoma 44As3-bearing nude mice. Tumor cells (44As3, 5.0×10^5) were transplanted into BLAB/C female nude mice ($n=6$) subcutaneously. BALB/c female nude mice bearing the 44As3 tumor were intravenously injected with Cderiv at a dose of 20 mg/kg at 10 days after the transplantation of 44As3 cells. ADR-micelles were injected at a dose of 10 mg/kg of physically entrapped ADR at 24 h after the Cderiv pretreatment. The mice in all cases were survived after the experiments finished at day 25. The tumor volumes and the body weights were measured at defined time intervals until 25 days after the drug treatments. The tumor volumes were calculated as follows: volume = $1/2LW^2$, where L is the long diameter and W is the short diameter of a tumor.

Animals

Five-week-old CDF_1 female mice were purchased from the Sankyo Labo Service Corporation, Tokyo, Japan. Six-week-old BALB/c female mice were purchased from CLEA Japan, Inc. All animal experiments were carried out in accordance with the guidelines of the Guiding Principles for the Care and Use of Laboratory Animals.

RESULTS AND DISCUSSION

Synthesis

Our polymeric micelle MRI contrast agent was used to observe the effect of Cderiv on tumor targeting. The Gd-DOTA-conjugated poly(ethylene glycol)-b-poly(L-lysine) block copolymer (PEG-P(Lys-DOTA-Gd)) formed a polymeric micelle as detected by means of DLS and GPC. This stably formed polymeric micelle exhibited both the characteristic long circulation in the blood and enough tumor accumulation to obtain MRI signals in the tumor tissue of colon 26-bearing mice, as reported previously (24). The blood half-lives of the polymeric micelle MRI contrast agent were 6.7 h and 18.4 h for α- and β-phases, respectively. This polymeric micelle MRI contrast agent exhibited pharmacokinetics behavior similar to that of an adriamycin-encapsulated polymeric micelle (ADR-micelle) (25,26). The advantage of this MRI contrast agent for the present work is that the MRI contrast agent informs us of the position and the amount of such a polymeric micelle MRI contrast agent in the tumor tissues, namely prediction of the drug targeting efficacy of ADR-micelle can be obtained.

Accumulation of Polymeric Micelles into Colon 26-Bearing Mice

Dose dependencies of Cderiv on tumor blood flow were evaluated previously (12). Intravenous injection of 1 and 3 mg/kg of Cderiv increased mean arterial blood pressure

for 2–3 h. The tumor blood flow was significantly decreased and was recovered in 2–4 h. However, the increased blood pressure at the dose of 10 mg/kg of Cderiv was maintained for 4–5 h, and the tumor blood flow was completely shut off among 8 h experiment. More than dose at 10 mg/kg of Cderiv caused long lasting tumor blood flow stasis for targeting of anticancer drug or diagnostic agent. Cderiv was intravenously injected at a dose of 20 mg/kg. The tumor blood flow stasis at this dose was reported to have continued for more than 6 h (13).

After the tumor blood flow stasis, some of the blood flows in the tumor vessels were recovered, and the others were not. Previous results showed that the Cderiv pretreatment remarkably enhanced permeability of the recovered and surviving tumor blood vessels (19). First, our polymeric micelle MRI contrast agent was injected at 72 h after Cderiv injection. The tumor tissues were taken out at 24 h after the contrast agent injection to determine gadolinium content in the tumor tissues by means of ICP measurement. As shown in Fig. 2a, significantly higher accumulation of the contrast agent was observed when Cderiv was pre-administered (9.8±0.8%ID/g for the Cderiv treatment (n=3) *vs* 5.6±1.0%ID/g tumor for the control (n=5), p value <0.001). This higher accumulation was due chiefly to the enhancement of the tumor vascular permeability induced by the Cderiv pretreatment, as observed in previous vital microscopic systems.

Then, time intervals of the Cderiv pretreatment were compared. When the polymeric micelle MRI contrast agent was injected at 24 h after the Cderiv pretreatment, 4.7±1.6%ID/g tumor tissues of the accumulation of the contrast agent were observed, as shown in Fig. 2b. However, when the contrast agent was injected at 72 h after the Cderiv injection, much higher accumulation in the tumor tissues was observed as described above (8.0± 2.5%ID/g tumor tissues). This lower accumulation of the contrast agent at 24 h was probably because of the ongoing blood flow stasis effect of Cderiv at this dose. Actually, the damage that the disrupting effect had on the tumor tissues was significant at 24 h after the Cderiv pretreatment in the case of the LY80 tumor model, and probably the contrast agent was not delivered effectively to tumor tissues because of poor tumor blood flow (19). However, at 72 h after the Cderiv pretreatment, the recovered tumor blood flow exhibited remarkable extravasation. This may explain why the polymeric micelle MRI contrast agent exhibited much higher accumulation in the tumor tissues at 72 h after the Cderiv pretreatment.

Enhancement of fluorescence intensities in the tumor tissues indicated the extravasation of FITC-labeled polymeric micelles from the tumor blood vessels (19); however, this fluorescence measurement was typically not quantitative analysis. Previous report used FITC-labeled polymeric micelles to observe the extravasation into tumor tissues. The polymeric micelle formed from FITC-labeled poly (ethylene glycol)-b-poly(b-benzyl L-aspartate) (PEG-PBLA-FITC, molecular weight, 15,300; Mw of PEG chain, 12,000; number of BLA units, 14.0). The size of FITC-labeled polymeric micelles exhibited 48.2±8.8 nm (the weight-average diameter ± SD). Enhancement of fluorescence intensities at both 24 h and 72 h after the pretreatment in the tumor tissues indicated the extravasation of FITC-labeled polymeric micelles from the tumor blood vessels (19); however, this fluorescence study was not of as quantitative measurements as measurements by means of ICP. Both cases exhibited the extravasation of FITC-labeled polymeric micelles; however, MRI as well as ICP measurement gave a quantitative amount of the polymeric micelle MRI contrast agent in the tumor tissues. Even though such fluorescence data exhibited the extravasation of polymeric micelles from the tumor blood vessels both 24 h and 72 h after the Cderiv treatment, the exact amount of the extravasated polymeric micelles in the tumor tissues was not measured. In contrast, the amount of the MRI contrast agent in tumor tissues at 72 h after the Cderiv pretreatment was quantitatively obtained through measurements of gadolinium amounts by means of ICP. A larger accumulation of 72 h post the Cderiv pretreatment was found than that of at 24 h, as shown in Fig. 2b. However, the nature of the tumor blood vessels' permeability by means of the Cderiv pretreatment remains unclear; it is thought to depend on tumor type and size. In colon 26 case, an accumulation of the polymeric micelle MRI contrast agent significantly enhanced at 72 h after the Cderiv pretreatment.

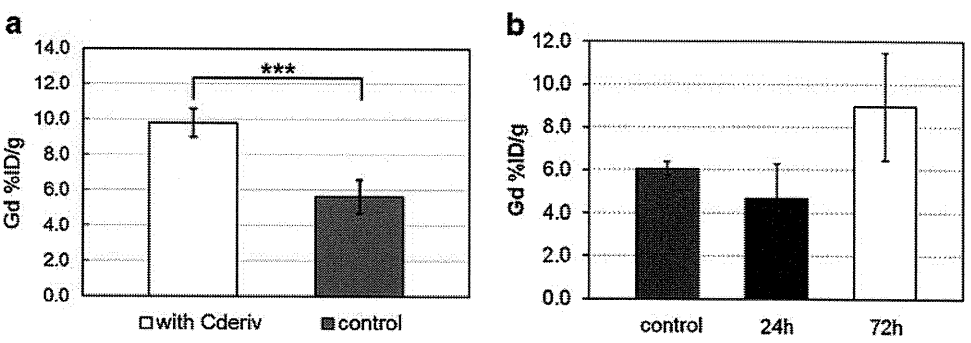

Fig. 2 Time interval effect of the Cderiv pretreatment on an accumulation of the polymeric micelle MRI contrast agent in colon 26 tumor tissues. (**a**) Either the Cderiv pretreatment at 72 h before the contrast agent injection (n=3) or without the treatment (n=5). (**b**) Control (n=3), the pretreatment at 24 h (n=4), and at 72 h (n=4), respectively. *** indicates P-value <0.001 (student's t-test).

MRI Study of Cderiv Pretreated Mice

Administration of Cderiv affected tumor vascular permeability, as we previously reported (19). An MRI study of the time interval study as shown in Fig. 2a was performed to observe accumulation of our polymeric micelle MRI contrast agent with the Cderiv pretreatment. When this contrast agent was used for tumor imaging in colon 26-bearing mice, a significant signal enhancement on the tumor T_1-weighted image was observed at 24 h (24). As described above section "Accumulation of Polymeric Micelles into Colon 26-Bearing Mice," in Fig. 2a, the significant difference of the accumulation of the contrast agent was found when Cderiv was pretreated at 72 h before the contrast agent injection. Figure 3 shows the axial T_1-weighted image of the tumor region (yellow circle) (a) with Cderiv treatment and (b) without treatment. A more than 2-fold (2.2 times) signal enhancement in the tumor region was observed at 24 h after the contrast agent injection (Fig. 3a). Without Cderiv treatment, 1.6 times of the signal enhancement was observed at 24 h after the injection compare to the before injection.

As well as the axial T_1-weighted image, the coronal slices exhibited characteristic images in the tumor tissues. Relatively high signal intensities were observed in the tumor-specific region, as shown in Fig. 4a (arrows). As compared to the coronal T_1-weighted images (Fig. 4a), the coronal T_2-weighted images also exhibited a curved-shape high-contrast region in the tumor tissues (Fig. 4b arrows). This relatively high contrast in the T_2-weighted image was observed before the injection of the contrast agent. Most likely, this region was caused by the Cderiv pretreatment resulting in a vasogenic edema formation. The whole mechanism of combretastatins including Cderiv on tumor vascularity is not still clear. However, evidence to date indicated the mechanism of combretastatins treatment. Combretastatins affected both morphological and functional changes in endothelial cells after the injection (9,17). Combretastatins act to the endothelial cell after the injection, which involves the damage and shape change of endothelial cells (15,16). The early effect after the combretastatin treatment on tumor vascularity was an increase in the permeability to macromolecules. This increase in the permeability leads to forming edema in tissues, and this could be increased in interstitial fluid pressure. Decreasing blood fluidity and stacking red blood cells were found in blood vessels. These events lead to vasoconstriction of the tumor vascularity.

Our previous report describes that surviving or restored tumor blood vessels exhibited a remarkable enhancement of permeability of FITC-labeled polymeric micelles after the Cderiv pretreatment (19). Figure 4c shows a merged image of the coronal T_1- or T_2-weighted tumor at the same position. The high-contrast region in the T_1-weighted image (arrow) was positioned adjacent to the T_2-weighted high-contrast region (arrow heads). These results support the assertion that the extravasation of the tumor blood vessels around such a T_2-high-contrast region was remarkably

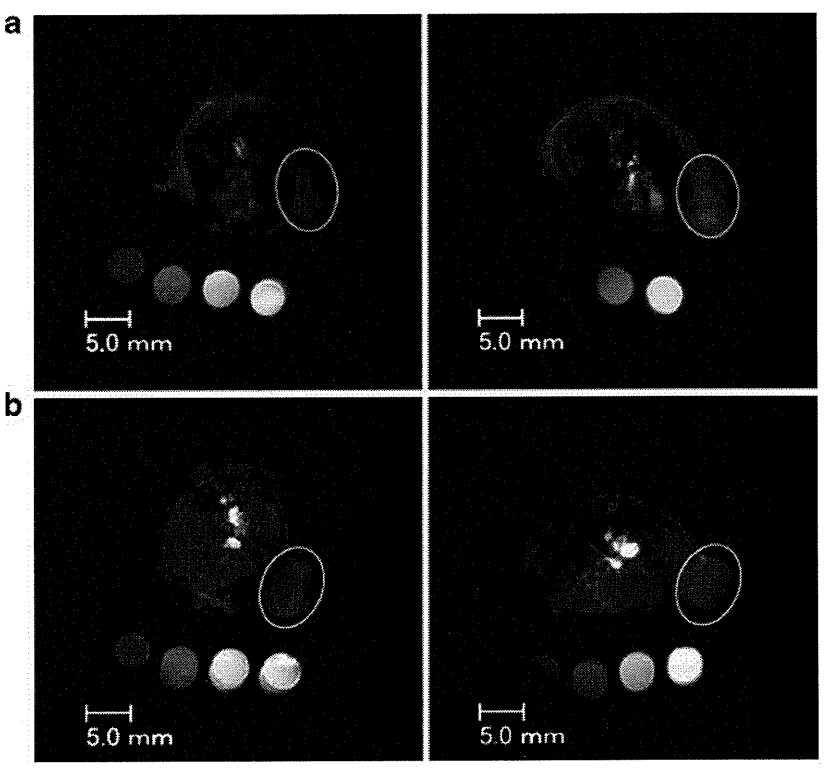

Fig. 3 Axial slices of the T_1-weighted MIP image of (**a**) Cderiv treatment at 72 h before the contrast agent injection (*left*) before and (*right*) 24 h, (**b**) without treatment (*left*) before and (*right*) 24 h.

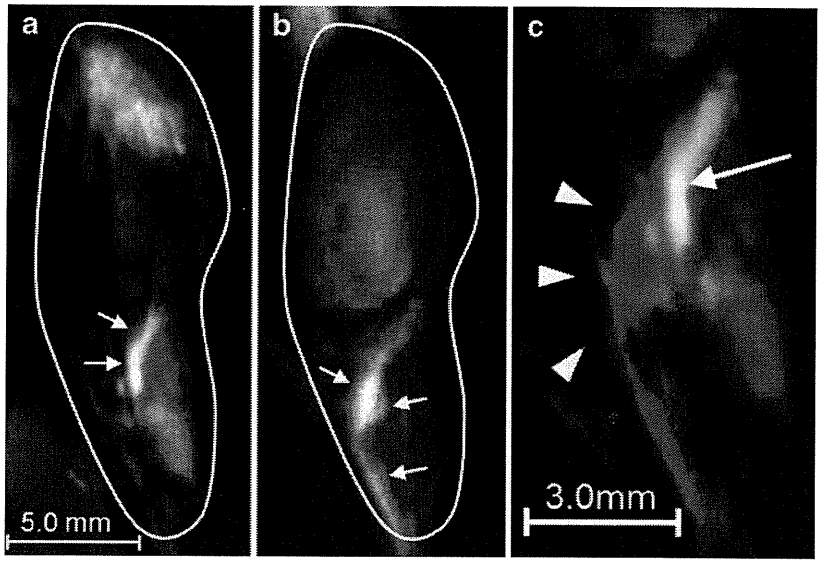

Fig. 4 Coronal slices of tumor area of (**a**) the T_1-weighted image and (**b**) the T_2-weighted image at 24 h after the injection. (**c**) A merged image of the T_1-weighted scenario (*gray*) and the T_2-weighted scenario (*magenta*) of the expanded tumor area. *Arrows* and *arrow heads* indicate the intense region of the T_1-weighted and the T_2-weighted images, respectively.

enhanced. One related result was a higher concentration of the polymeric micelle MRI contrast agent in the tumor tissues. So far, there have been no reports of an accumulation of nanoparticles specific-regions in tumor by means of the EPR effect. In terms of tumor diagnosis, high concentrations of the MRI contrast agent in such a part of the region led to the intense signal compared with the case of homogeneous distribution in a whole region of the tumor tissues. In this report, a higher accumulation of the MRI contrast agent in the tumor tissues was obtained by means of the Cderiv pretreatment. Furthermore, such a extravasated MRI contrast agent was locally concentrated in the specific region in which Cderiv might be worked. In general, the MRI contrast agent exhibits the T_1-shortening property of water protons. The concentration of the gadolinium ion significantly affected the T_1-shortening property, which would lead to the intense signal. Consequently, the observations in such specific contrast enhancement at the solid tumor help to distinguish the normal and the diseased tissues easily.

Anticancer drugs should be distributed through the whole region of the tumor tissues. Our previous report indicates that movements of macromolecules including polymeric micelles are strongly dependent on a perfusion of the tumor tissues. Namely, tumor-tissue perfusion can distribute a locally accumulated polymeric micelle encapsulating anticancer drug in the tumor tissues.

As we described in the introduction, the Cderiv pretreatment enhances the vascular permeability of the solid tumor even in microscopic tumors. In recent reports on tumor permeability for a drug targeting system, a tumor environment change by a TGF-β receptor inhibitor (TβRI) emerged for the EPR effect enhancement. TβRI induced alternation of tumor neovasculature that lead to enhanced permeability of nanoparticles (29,30). However, function of TGF-β inhibitor is diverse, and the use of such a TGF-β inhibitor for tumor permeability must carefully address the dose and side effect. On the other hand, nitroglycerin, classical medication for angina topically or orally, was examined for the EPR effect

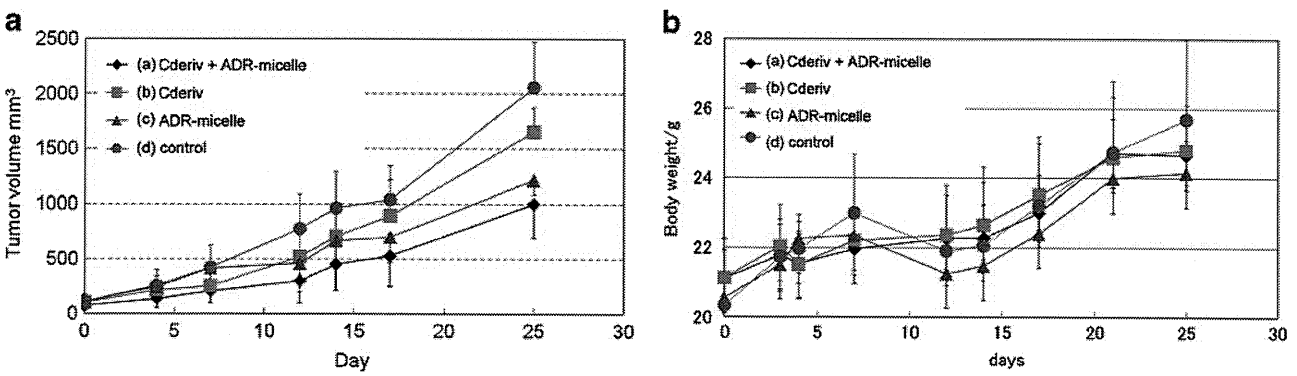

Fig. 5 (**a**) Antitumor activity of 44As3-bearing mice ($n = 6$) and (**b**) the body weight change after a single injection of (a) Cderiv + ADR-micelle, (b) Cderiv, (c) ADR-micelle, and (d) control.

enhancement. Topical application of nitroglycerin that converts to nitric oxide enhanced tumor permeability for targeting of macromolecular antitumor drugs (31,32). In contrast, Cderiv acts as a vascular disrupting agent at the tumor-specific blood capillaries. An anticancer drug targeting system supported with the Cderiv pretreatment can overcome a problem with the delivery of the nanocarriers. Because the delivery of anticancer drugs would strongly depend on the tumor vascular system, the tumor blood vessels would need to be opened to extravasate the nanocarriers. This combination greatly enhanced their permeability, resulting in the high accumulation in the solid tumor. Also, when locally accumulated, the contrast agent exhibited a relatively high signal-to-noise (S/N) ratio. This was the case of the MRI contrast agent; however, a polymeric micelle encapsulating anticancer drug could accumulate with the Cderiv pretreatment.

Antitumor Activity Relates to the Cderiv Pretreatment with ADR-Micelles Targeting 44As3 Human Gastric Scirrhous Carcinoma-Bearing Mice

Diagnosis of this scirrhous gastric carcinoma is quite difficult because of pathological features of this gastric cancer in humans. Highly progressed peritoneal dissemination or distant metastasis to lymph nodes has been observed in many cases. Due to a problem of anticancer drug targeting into this gastric cancer, this gastric scirrhous carcinoma usually generates a poor prognosis even after resection in humans. Targeting of anticancer drug into such tumor model has been highly desired (33). Antitumor activity of a single injection of ADR-micelle with the Cderiv pretreatment in 44As3 human gastric scirrhous carcinoma was evaluated by monitoring of tumor growth, as shown in Fig. 5. The dose of Cderiv and the dose of ADR-micelles were 20 mg/kg and 10 mg/kg, respectively.

Cderiv itself exhibited antitumor activity by disrupting tumor blood vessels. ADR-micelles exhibited better antitumor activity than the Cderiv treatment alone. To observe the antitumor activity, the current study used a combination of the Cderiv pretreatment with ADR-micelles. There was no statistically significant difference between the combination of Cderiv with ADR-micelles and ADR-micelles; however, this result indicates that the combination was effective for suppressing tumor growth.

In this animal experiment, we injected 10 mg/kg of ADR-micelles at 24 h after the Cderiv pretreatment. We observed enhancement of tumor permeability in LY80 tumors when Cderiv was administered at 24 h before the FITC-micelle injection (19). However, from the biodistribution study of the polymeric micelle MRI contrast agent, the contrast agent accumulated much higher concentration in the tumor tissues when Cderiv was pretreated at 72 h before the injection. In this 44As3 case, the tumor blood flow may not be recovered at 24 h after the Cderiv treatment. The effects of Cderiv on each tumor models were not known in the appropriate time to pre-treat before ADR-micelle injection.

So far, this experiment did not show serious side effects with a multiplier anticancer drug combination. In terms of the body-weight change, no difference was observed to compare with the control and the others, as shown in Fig. 5b. This combination might have an optimum time interval and dose for the antitumor activity. Also, detailed movements of the polymeric micelles after local accumulation in the tumor tissues are not yet clear; however, this combination may have a chance to be a new concept underlying nanocarrier-based antitumor drug targeting systems.

CONCLUSION

A vascular disrupting agent, Cderiv, enhanced the tumor accumulation of a polymeric micelle MRI contrast agent in the tumor tissues. An MRI shows that the signal intensities of the T_1-weighted images of the tumor area greatly enhanced at 24 h after the MRI contrast agent injection. The MRI study indicates that there was observable local accumulation of the polymeric micelles in the tumor-specific region which led to relatively high signal intensity in the tumor tissues. This T_1-relatively high region was positioned adjacent to the T_2-weighted high-contrast region. The pretreatment of Cderiv changed the tumor environment, leading to extravasation of the polymeric micelles in the tumor tissues. The combination of the Cderiv pretreatment and ADR-micelles exhibited better tumor-growth suppression of 44As3 human gastric scirrhous carcinoma. The Cderiv pretreatment enhanced tumor accumulation of the polymeric micelle MRI contrast agent. We expect a combination therapy of a polymeric micelle anti cancer drug with the Cderiv pretreatment can exhibit greater antitumor activity than a single agent's therapy through optimization in doses of both agents as well as in the interval between the two agents' injections.

REFERENCES

1. Matsumura Y, Maeda H. A new concept for macromolecular therapeutics in cancer chemotherapy: mechanism of tumoritropic accumulation of proteins and the antitumor agent Smancs. Cancer Res. 1986;46:6387–92.
2. Aliabadi HM, Lavasanifar A. Polymeric micelles for drug delivery. Expert Opin Drug Deliv. 2006;3(1):130–62.

3. Torchilin V. Tumor delivery of macromolecular drugs based on the EPR effect. Adv Drug Deliv Rev. 2011;63:131–5.
4. Amantea MA, Forrest A, Northfelt DW, Nanelok R. Population pharmacokinetics and pharmacodynamics of pegylated-liposomal doxorubicin in patients with AIDS-related Kaposi's sarcoma. Clin Pharmcol Ther. 1997;61:301–11.
5. Duncan R. Polymer conjugates as anticancer nanomedicines. Nat Rev Cancer. 2006;6:688–701.
6. Duncan R. The dawning era of polymer therapeutics. Nat Rev Drug Discov. 2003;2:347–60.
7. Hori K, Nishihara M, Yokoyama M. Vital microscopic analysis of polymeric micelle extravasation from tumor vessels: macromolecular delivery according to tumor vascular growth stage. J Pharm Sci. 2009;99(1):549–62.
8. Pettit GR, Singh SB, Hamel E, Lin CM, Alberts DS, Garcia-Kendall D. Isolation and structure of the strong cell growth and tubulin inhibitor combretastatin A-4. Experientia. 1989;45(2):209–11.
9. Tozer GM, Kanthou C, Parkins CS, Hill SA. The biology of the combretastatins as tumour vascular targeting agents. Int J Exp Pathol. 2002;83(1):21–38.
10. Hatanaka T, Fujita K, Ohsumi K, Nakagawa R, Fukuda Y, Nihei Y, *et al.* Novel B-ring modified combretastatin analogues: syntheses and antineoplastic activity. Bioorg Med Chem Lett. 1998;8(23):3371–4.
11. Ohsumi K, Nakagawa R, Fukuda Y, Hatanaka T, Morinaga Y, Nihei Y, *et al.* Novel combretastatin analogues effective against murine solid tumors: design and structureactivity relationships. J Med Chem. 1998;41(16):3022–32.
12. Hori K, Saito S, Nihei Y, Suzuki M, Sato Y. Antitumor effects due to irreversible stoppage of tumor tissue blood flow: evaluation of a novel combretastatin A-4 derivative, AC7700. Jpn J Cancer Res. 1999;90 (9):1026–38.
13. Hori K, Saito S. Microvascular mechanisms by which the combretastatin A-4 derivative AC7700 (AVE8062) induces tumour blood flow stasis. British J Cancer. 2003;89:1334–44.
14. Hori K. Cancer therapy by means of irreversible tumor blood flow stasis: Starvation tactics against solid tumors. Gene Ther Mol Biol. 2005;9:203–16.
15. Tozer GM, Kanthou C, Baguley BC. Disrupting tumour blood vessels. Nat Rev Cancer. 2005;5:423–35.
16. Griggs J, Metcalfe JC, Hesketh R. Targeting tumour vasculature: the development of combretastatin A4. Lancet Oncol. 2001;2(2):82–7.
17. Tozer GM, Prose VE, Wilson J, Cemazar M, Shan S, Dewhirst ME, *et al.* Mechanism associated with tumor vascular shut-down induced by combretastatin A-4 phosphate: intravital microscopy and measurement of vascular permeability. Cancer Res. 2001;61:6413–22.
18. Kim TJ, Ravoori M, Landen CN, Kamat AA, Han LY, Lu C, *et al.* Antitumor and antivascular effects of AVE8062 in ovarian carcinoma. Cancer Res. 2007;67(19):9337–45.
19. Hori K, Nishihara M, Shiraishi K, Yokoyama M. The combretastatin derivative (Cderiv), a vascular disrupting agent, enables polymeric nanomicelles to accumulate in microtumors. J Pharm Sci. 2010;99(6):2914–25.
20. Veiseh O, Gunn JW, Zhang M. Design and fabrication of magnetic nanoparticles for targeted drug delivery and imaging. Adv Drug Deliv Rev. 2010;62(3):284–304.
21. Sun C, Lee JSH, Zhang M. Magnetic nanoparticles in MR imaging and drug delivery. Adv Drug Deliv Rev. 2008;60(11):1252–65.
22. Liu Y, Miyoshi H, Nakamura M. Nanomedicine for drug delivery and imaging: A promising avenue for cancer therapy and diagnosis using targeted functional nanoparticles. Int J Cancer. 2007;120(2):2527–37.
23. Caravan P, Ellison JJ, McMurry TJ, Lauffer RB. Gadolinium(III) chelates as MRI contrast agents: structure, dynamics, and applications. Chem Rev. 1999;99(9):2293–352.
24. Shiraishi K, Kawano K, Minowa T, Maitani Y, Yokoyama M. Preparation and *in vivo* imaging of PEG-poly(L-lysine)-based polymeric micelle MRI contrast agents. J Contr Release. 2009;136(1):14–20.
25. Yokoyama M, Okano T, Sakurai Y, Fukushima S, Okamoto K, Kataoka K. Selective delivery of adriamycin to a solid tumor using a polymeric micelle carrier system. J Drug Targeting. 1999;7(3):171–86.
26. Yokoyama M, Miyauchi M, Yamada N, Okano T, Sakurai Y, Kataoka K. Characterization and antitumor activity of the micelle-forming polymeric anticancer drug adriamycin-conjugated poly (ethylene glycol)-poly(aspartic acid) block copolymer. Cancer Res. 1999;50:1693–700.
27. Yanagihara K, Takigahira M, Tanaka H, Komatsu T, Fukumoto H, Koizumi F, *et al.* Development and biological analysis of peritoneal metastasis mouse models for human scirrhous stomach cancer. Cancer Sci. 2004;96(6):323–32.
28. Yokoyama M, Fukushima S, Uehara R, Okamoto K, Kataoka K, Sakurai Y, *et al.* Characterization of physical entrapment and chemical conjugation of adriamycin in polymeric micelles and their design for *in vivo* delivery to a solid tumor. J Contr Release. 1998;50(1–3):79–92.
29. Kano RM, Bae Y, Iwata C, Morishita Y, Yashiro M, Oka M, *et al.* Improvement of cancer-targeting therapy, using nanocarriers for intractable solid tumors by inhibition of TGF-β signaling. Proc Natl Acad Sci USA. 2007;104(9):3460–5.
30. Minowa T, Kawano K, Kuribayashi H, Shiraishi K, Sugino T, Hattori Y, *et al.* Increase in tumour permeability following TGF-β type I receptorinhibitor treatment observed by dynamic contrast-enhanced MRI. Br J Canc. 2009;101:1884–90.
31. Seki T, Fang J, Maeda H. Enhanced delivery of macromolecular antitumor drugs to tumors by nitroglycerin application. Cancer Sci. 2009;100(12):2426–30.
32. Maeda H. Tumor-selective delivery of macromolecular drugs via the EPR effect: background and future prospects. Bioconjugate Chem. 2010;21(5):797–802.
33. Nakajima TE, Yanagihara K, Takigahira M, Yasunaga M, Kato K, Hamaguchi M, *et al.* Antitumor Effect of SN-38–releasing polymeric micelles, NK012, on spontaneous peritoneal metastases from orthotopic gastric cancer in mice compared with irinotecan. Cancer Res. 2008;68(22):9318–22.

IOP PUBLISHING PHYSICS IN MEDICINE AND BIOLOGY

Phys. Med. Biol. **57** (2012) 2039–2061 doi:10.1088/0031-9155/57/7/2039

Statistical image reconstruction from limited projection data with intensity priors

Essam A Rashed[1,2] **and Hiroyuki Kudo**[1]

[1] Department of Computer Science, Graduate School of Systems and Information Engineering, University of Tsukuba, Tennoudai 1-1-1, Tsukuba 305-8573, Japan
[2] Department of Mathematics, Faculty of Science, Suez Canal University, Ismailia 41522, Egypt

E-mail: essam@imagelab.cs.tsukuba.ac.jp

Received 30 September 2011, in final form 15 January 2012
Published 20 March 2012
Online at stacks.iop.org/PMB/57/2039

Abstract

The radiation dose generated from x-ray computed tomography (CT) scans and its responsibility for increasing the risk of malignancy became a major concern in the medical imaging community. Accordingly, investigating possible approaches for image reconstruction from low-dose imaging protocols, which minimize the patient radiation exposure without affecting image quality, has become an issue of interest. Statistical reconstruction (SR) methods are known to achieve a superior image quality compared with conventional analytical methods. Effective physical noise modeling and possibilities of incorporating priors in the image reconstruction problem are the main advantages of the SR methods. Nevertheless, the high computation cost limits its wide use in clinical scanners. This paper presents a framework for SR in x-ray CT when the angular sampling rate of the projection data is low. The proposed framework is based on the fact that, in many CT imaging applications, some physical and anatomical structures and the corresponding attenuation information of the scanned object can be *a priori* known. Therefore, the x-ray attenuation distribution in some regions of the object can be expected prior to the reconstruction. Under this assumption, the proposed method is developed by incorporating this prior information into the image reconstruction objective function to suppress streak artifacts. We limit the prior information to only a set of intensity values that represent the average intensity of the normal and expected homogeneous regions within the scanned object. This prior information can be easily computed in several x-ray CT applications. Considering the theory of compressed sensing, the objective function is formulated using the ℓ_1 norm distance between the reconstructed image and the available intensity priors. Experimental comparative studies applied to simulated data and real data are used to evaluate the proposed method. The comparison indicates a significant improvement in image quality when the proposed method is used.

(Some figures may appear in colour only in the online journal)

1. Introduction

X-ray computed tomography (CT) imaging is generally used for the reconstruction of an object function from its projection data. The projection data, measured by a detector array, represents the internal structure through the attenuation map of the x-ray photons. The sampling rate and data-acquisition orbit have a strong influence on the exactness and stability of the image reconstruction process. It is well known that under-sampling of projection views converts the image reconstruction inverse problem into the ill-posed one (Natterer 1986, Herman and Kuba 1999), where the reconstructed image suffers from different types of image artifacts that vary according to the availability of projection data (Joseph and Schulz 1980, Rangayyan *et al* 1985). A common data limitation problem in clinical and industrial applications is the limited view problem. The term *limited view*, which is also called *sparse projections*, refers to the case where the measured projection data are obtained over a small number of equally/unequally distant angles less than what is traditionally required by the Nyquist sampling rule (Natterer 1986). In medical imaging, as well as several industrial applications, it is required to reconstruct an artifact-free image from a limited view projection data. When the target object is presented in the binary form (e.g. 0/1), exact reconstruction can be achieved from small number of projections (Herman and Kuba 2007). Unfortunately, this assumption is not valid in several real CT applications. The problem of image reconstruction from small projections had been studied, and many reconstruction algorithms are already proposed in the literature; see e.g. Huesman (1977), Brooks *et al* (1979), Nassi *et al* (1982), Payot *et al* (1997), Galigekere *et al* (1999), Li *et al* (2004), Sidky *et al* (2006), Herman and Davidi (2008) and Hansis *et al* (2008).

The wide spread of the x-ray CT scanners worldwide and their extensive usage in medical diagnosis for many diseases has led to a significant dose increase to the community. The minimization of radiation exposure in CT imaging had become a key requirement in many imaging applications, especially for pediatric (Brenner and Hall 2007, Yu *et al* 2009). For example, in image-guided radiation therapy (IGRT), patients are usually subject to multiple scans that accumulate the dose to a risky level. However, decreasing x-ray beam intensity usually increases the statistical noise in the reconstructed images, which reduces the ability to extract useful information from these images. One potential approach that achieves the objective of ionizing radiation reduction, while providing patients with more comfortable short time imaging, is to under-sample the number of projection views.

Statistical reconstruction (SR) has been used for a long time in emission tomography for its ability to reduce statistical noise in reconstructed images. The correct noise modeling and the ability to incorporate *a priori* information in the image reconstruction objective function are the key reasons for being used in several in-duty PET and SPECT imaging equipments. However, in x-ray CT, conventional methods derived from analytical inversion formulae, such as the standard filtered backprojection (FBP), are still the methods of choice in clinical scanners. The main reason is the expensive computation cost of SR methods when it is applied to relatively large photon counts used in x-ray CT. Recently, the use of SR in transmission CT has taken much interest due to the rapid growth of the computing power and the use of high-speed GPU processing units in image reconstruction.

In CT imaging, we measure the attenuation of x-ray within the scanned object. In this imaging modality, it is known that the variation of the attenuation coefficients, which is also called intensity, within the same homogenous object is rather small. The incorporation of *a priori* known information, to improve images reconstructed from limited projection data in CT, has been extensively studied in the past two decades; see, e.g., Sauer *et al* (1994), Kolehmainen *et al* (2003), Siltanen *et al* (2003), Chen *et al* (2008), Leng *et al* (2008) and Rashed and Kudo (2011). The nature of the prior information required for exact reconstruction

is not clear yet. Thus, it is interesting to quantitatively investigate how different types of prior information contribute to the image quality in various data limitation problems. We can classify the possible prior information into the following three categories: (1) full reference image (intensity value + pixel position), (2) boundaries and support information (pixel position only) and (3) attenuation information (intensity value only). The first category considers the case where *a priori* information is obtained from a reference image generated prior to the reconstruction. The term reference image usually refers to an image that includes basic and normal structures of the scanned object. Reference image may be obtained through an earlier scan of the patient, segmentation of neighboring slices or a blurred image reconstructed from all measured projection data in gated-CT. The second category describes the use of *a priori* information corresponding to the boundaries of uniform regions without further spatial information. This includes the well-known quadratic smoothing penalty. The third category corresponds to the case where *a priori* information is limited to a set of intensity values representing uniform regions of the object without additional knowledge about the pixel positions. In this work, we study the use of prior information corresponding to the third category.

In this paper, we propose a Bayesian framework for SR from limited view projection data. We assume that a small number of intensity values that represent the average value of expected homogeneous regions (organs) are *a priori* known or estimated with high accuracy. For convenience, we refer to this prior information as intensity prior throughout the paper. We design the objective function such that it includes a distance function based on the ℓ_1 norm to the intensity prior. The resulting SR method is evaluated using simulated data and real data with different settings for the prior.

This paper is organized as follows. In section 2, we briefly introduce the imaging model for SR in transmission CT. The proposed approach is detailed, and the image reconstruction algorithm is developed in section 3. The experimental data are presented and analyzed in section 4 and followed by the discussion and conclusion in section 5.

2. Imaging model for SR

2.1. Statistical image reconstruction

In transmission CT, the x-ray beam is radiated to the target object where a portion of the radiation is absorbed by the object while the remaining portion transmits through it. The transmitted portion of the radiated photons is measured by an array of detectors located on the opposite side of the x-ray tube. The attenuation map μ of the object can be identified according to Beer's law of attenuation (Lange and Carson 1984):

$$I = I_0 \exp\left(-\int_s \mu \, \mathrm{d}s\right), \tag{1}$$

where I and I_0 are the photon counts, and the blank scan measured at a single detector bin, respectively, with s represents the virtual ray path from the tube focal point to the detector bin. Assuming that the attenuation value is constant within small size image pixels, the transmission x-ray CT can be described in a discrete form using the following statistical model:

$$y_i \approx \text{Poisson}\left(b_i \exp\left(-\sum_{j=1}^{n} a_{ij}\mu_j\right)\right), \tag{2}$$

where $\mu = (\mu_1, \ldots, \mu_n)$ is the image vector representing the attenuation coefficients of the imaged object, $y = (y_1, \ldots, y_m)$ is a vector representing the raw detector measurements with

the corresponding blank scan $b = (b_1, \ldots, b_m)$ and $A = \{a_{ij}\}$ is the $m \times n$ system matrix that models the imaging system. In the statistical model in equation (2), we consider the use of a monochromatic x-ray spectrum and ignore the effect of scattered photons, for simplicity. The log-likelihood function for the observed photon counts, as described in the literature, is given by

$$l(\mu) = -L(\mu) = \sum_{i=1}^{m} \left[y_i \log(b_i) - y_i \sum_{j=1}^{n} a_{ij}\mu_j - \log(y_i!) - b_i \exp\left(- \sum_{j=1}^{n} a_{ij}\mu_j \right) \right]. \quad (3)$$

The solution of the image reconstruction problem is found through a maximization of the log-likelihood function after ignoring the irrelevant terms. The maximum likelihood solution of the SR problem is found by

$$\mu^* = \arg\min_{\mu \geqslant 0} L(\mu), L(\mu) = \sum_{i=1}^{m} [b_i \exp(-\langle a_i, \mu \rangle) + y_i \langle a_i, \mu \rangle], \quad (4)$$

where $\langle a_i, \mu \rangle = \sum_{j=1}^{n} a_{ij}\mu_j$ is the inner product of the ith row of matrix A and image vector μ. When the acquired data y are limited such that $m \ll n$, the image reconstruction becomes an ill-posed problem and achieving a reliable and feasible solution is challenging. To overcome this problem, the well-known Bayesian methods, that include *a priori* information on the scanned object, are used. The solution of the image reconstruction problem is found through maximizing the *a posteriori* (MAP) function:

$$P(\mu|y) = \frac{P(y|\mu)P(\mu)}{P(y)}, \quad (5)$$

and the maximum *a priori* solution of the reconstruction problem is found by

$$\mu^* = \arg\min_{\mu \geqslant 0} f_\beta(\mu), f_\beta(\mu) = L(\mu) + \beta U(\mu), \quad (6)$$

where $U(\mu)$ is known as the penalty term or the regularization function that presents prior knowledge of the image object and β is a hyper-parameter that controls the power of the regulation term.

2.2. *Compressed sensing*

Since the introduction of the compressed sensing (CS) principle (Candès *et al* 2006, Donoho 2006), several approaches were presented to solve the inverse problem for image reconstruction from a small number of projection views. The main approach is based on the minimization of the objective function that includes the ℓ_1/ℓ_0 norm of a sparse representation of the target object. This formulation of the objective function can effectively find the sparse solution from feasible ones. When the object is presented in a sparse form, the number of projections required for a good estimation is significantly less than that of the traditional Nyquest sampling criteria. This approach was presented early and was used to develop an image reconstruction algorithm for blood vessel imaging from a small number of projection views (Li *et al* 2002). When the target object is originally sparse, the image reconstruction problem is formulated generally as the minimization of $N(\mu)$ subject to data fidelity terms where $N(\cdot)$ is a norm function such as ℓ_1/ℓ_0 norm. However, in many cases of x-ray CT applications, the target object is non-sparse. The image reconstruction problem is then formulated to minimize $N(\Phi(\mu))$, where $\Phi(\cdot)$ is a sparsification transform such as the general gradient, wavelets or total-variation (TV) norm. The TV norm was introduced for the first time by Rudin *et al* (1992) as an effective tool for image denoise. The TV norm is known for its edge preservation property providing that it is based on the non-quadratic function and this is the main reason that TV-based image

reconstruction algorithms have gained much attention recently. For example, it is used for SPECT imaging (Persson *et al* 2001), Cone-beam CT (Sidky and Pan 2008) and cardiac gated micro-CT (Song *et al* 2007). Interesting comparison studies between the TV-based approaches and SR methods were recently presented by Tang *et al* (2009) and Bian *et al* (2010).

However, the use of straight TV models for realistic image reconstruction has been shown to produce artificial patches that reduce the image quality and their possibility to be used in clinical equipment as well (Fahimian *et al* 2010). Furthermore, it is known that TV-based methods may result in losing small size and low-contrast structures during the reconstruction. Moreover, the TV-minimization is usually implemented through iteration procedures, which considerably increase the computation cost of the image reconstruction process, especially in 3D/4D reconstruction. In general, when the projection data are highly under-sampled, the image reconstruction becomes an underdetermined problem and the achievement of exact reconstruction is not theoretically possible (Herman and Davidi 2008). Additional terms, added to the objective function, can lead to a more accurate reconstruction. Here, we introduce a simple and easy-to-compute prior information which we call intensity prior. As will be shown later through the experimental studies, intensity prior can be easily estimated, and it contributes effectively to the image quality without affecting the contrast.

2.3. MAP reconstruction and intensity prior

The penalty term $U(\mu)$ in equation (6) can be formulated using several approaches. It is common in nuclear imaging to introduce a penalty term in the image reconstruction objective function for the benefit of obtaining a data consistent image with less noise. However, it is difficult to introduce *a prior* knowledge that fits with the imaging applications. For example, a commonly used quadratic smoothing penalty is defined as

$$U(\mu) = \sum_{j,j' \in C} \omega_{j,j'} (\mu_j - \mu_{j'})^2, \tag{7}$$

where C is a set of neighboring pixels and $\omega_{j,j'}$ is a weight assigned to each pair of pixels (j, j'). Using the quadratic smoothing penalty can effectively suppress noise but on the expense of preserving sharp edges.

In this paper, we introduce the penalty term as a distance function between the reconstructed image μ and the available intensity values. In x-ray CT, the attenuation coefficients within the same region (organ) are almost uniform and can be *a priori* known within a specific range that slightly varies based on the imaging application. For example, it is not difficult to estimate, with high accuracy, the attenuation coefficients of normal organs appearing in a chest CT imaging of a mature patient. The distance function can take various forms based on image properties and the nature of available *a priori* information. Considering the intensity prior, the proposed distance function is formulated as

$$U(\mu) \equiv D(\mu, z) = \sum_{j=1}^{n} \min_{l=1}^{L} [\omega_l d(\mu_j, z_l)], \tag{8}$$

where $z = (z_1, \ldots, z_L)$ are the known intensity values arranged in ascending order (i.e. $z_1 < z_2 < \ldots < z_L$), $\omega_1, \ldots, \omega_L$ is a set of empirically determined parameters that quantitatively represent the corresponding intensity values, and $d(\cdot, \cdot)$ is a single-variable distance function. This distance function should be carefully selected because it has a strong influence on the quality of the reconstructed image. A possible useful choice is the ℓ_1 norm distance such that

$$d(a, b) = |a - b|. \tag{9}$$

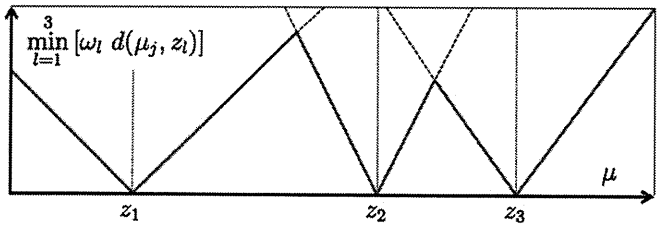

Figure 1. The proposed penalty function in equation (8) corresponding to $L = 3$.

The most advantageous feature, of the proposed penalty function in equation (8), is that the required *a priori* information is limited to only a small number of intensity values, which can be easily available in several clinical applications. An illustration of the proposed penalty function is shown in figure 1.

3. Methods

3.1. Reconstruction algorithm

The main difficulty in minimizing the objective function in equation (6) is that the proposed penalty term in equation (8) is based on the ℓ_1 norm, which is neither convex nor differentiable. Therefore, it is not possible to use the ordinary gradient-type iterative method to optimize the objective function. Alternatively, the well-known majorization–minimization (MM) strategy (Fessler and Hero 1995, Daubechies *et al* 2004) is used to derive a separable quadratic function. At each iteration k, the non-separable part of the main objective function in equation (6) is approximated by a separable quadratic function $\tilde{L}(\mu; \mu^k)$ around $\mu = \mu^k$ such that

$$\tilde{L}(\mu^k; \mu^k) = L(\mu^k), \tag{10}$$

$$\partial \tilde{L}(\mu; \mu^k)/\partial \mu_j|_{\mu=\mu^k} = \partial L(\mu)/\partial \mu_j|_{\mu=\mu^k}. \tag{11}$$

The approximate quadratic majorization to $L(\mu)$ is formulated as

$$\tilde{L}(\mu; \mu^k) = L(\mu^k) + \nabla L(\mu)|_{\mu=\mu^k}(\mu - \mu^k)^\top + \frac{1}{2} Q(\mu^k)(\mu_j - \mu_j^k)^2 \tag{12}$$

$$= \frac{1}{2} \sum_{j=1}^{n} \frac{\sum_{i=1}^{m} a_{ij} \langle a_i, \mu^k \rangle b_i \exp(-\langle a_i, \mu^k \rangle)}{\mu_j^k} (\mu_j - p_j)^2 + T(\mu^k), \tag{13}$$

where $T(\mu^k)$ is the term independent of μ,

$$Q(\mu^k) = \sum_{j=1}^{n} \frac{\sum_{i=1}^{m} a_{ij} \langle a_i, \mu^k \rangle b_i \exp(-\langle a_i, \mu^k \rangle)}{\mu_j^k}, \tag{14}$$

and

$$p_j = \mu_j^k + \mu_j^k \frac{\sum_{i=1}^{m} a_{ij}(b_i \exp(-\langle a_i, \mu^k \rangle) - y_i)}{\sum_{i=1}^{m} a_{ij} \langle a_i, \mu^k \rangle b_i \exp(-\langle a_i, \mu^k \rangle)}. \tag{15}$$

The resulting separable objective function $\tilde{f}_\beta(\mu; \mu^k) = \tilde{L}(\mu; \mu^k) + \beta U(\mu)$ is minimized analytically to obtain the next iterate μ^{k+1}. This approximation is useful to obtain a separable objective function when the penalty term is non-differentiable such as the case of ℓ_1 norm

distance. We consider the proposed penalty term of intensity information in equation (8), in which the separable objective function $\tilde{f}_\beta(\mu; \mu^k)$ can be written as

$$\tilde{f}_\beta(\mu; \mu^k) = \sum_{j=1}^{n} \beta\omega_h[c_{j,h}(\mu_j - p_j)^2 + d(\mu_j, z_h)] + T(\mu^k), \tag{16}$$

$$h = \{h \in \{1, \ldots, L\} : d(\mu_j, z_h) = \min_{l=1}^{L} d(\mu_j, z_l)\},$$

$$c_{j,h} = \frac{1}{2\beta\omega_h\mu_j^k} \sum_{i=1}^{m} a_{ij}\langle a_i, \mu^k\rangle b_i \exp(-\langle a_i, \mu^k\rangle). \tag{17}$$

The proposed algorithm, which we called intensity-based MAP (iMAP), for transmission tomography is implemented through the following steps.

(i) (Initialization step) Estimate the intensity prior $z = (z_1, \ldots, z_L)$, set the initial image μ^0 to a uniform positive value and set the iteration number $k \to 0$.
(ii) (Majorization step) The objective function $f(\mu)$ is approximately majorized around the current estimate μ^k using equation (13) to the separable function in equation (16).
(iii) (Minimization) The separable objective function $\tilde{f}(\mu; \mu^k)$ is minimized over $\mu \geqslant 0$ to obtain the image estimate μ^{k+1} in the next iterate:

$$q = \arg\min_{\mu \geqslant 0} \tilde{f}_\beta(\mu; \mu^k), \quad \mu_j^{k+1} = \max(q_j, \epsilon), \tag{18}$$

where ϵ is a small value to guarantee that $\mu_j^{k+1} > 0$.
(iv) (Iterate condition) Set iteration number $k \to k+1$, and repeat steps (i)–(iii) until reaching a stopping criterion.

The main theoretical framework for the derivation of the iMAP algorithm is the same as that presented in the earlier work for the anatomical-MAP-EM method for PET/SPECT imaging (Mameuda and Kudo 2007). However, the present method investigates a different imaging problem in transmission CT, where the essential target of the previous work was to reconstruct PET/SPECT images with better noise/contrast properties. Moreover, the intensity prior, which is more appropriate for the transmission CT imaging, is an original contribution of this paper.

It is known that in the generic ℓ_1 norm prior, the convergence of the iterative algorithm is guaranteed (Daubechies *et al* 2004, Loris 2009). In this paper, we have used the MM strategy to generate an approximate separable function for which the convergence properties of the proposed algorithm are not clear. However, the same framework can be used with the exact surrogate function presented by Erdŏgan and Fessler (1999). In this case, the algorithm monotonically decreases the objective function toward a local minimum. Nevertheless, as the objective function is non-convex, there is no proof that the algorithm will achieve the global convergence. Recently, it has become interesting to study the performance of similar algorithms and some papers have discussed the convergence properties of iterative hard thresholding (e.g. Blumensath and Davies 2010).

3.2. Intensity multi-thresholding

The minimization in equation (18) can now be implemented directly. It is easy to prove that the optimization of the following simple separable objective function:

$$x^* = \arg\min_x \frac{\alpha}{2}(x - a)^2 + \beta|x - b|, \tag{19}$$

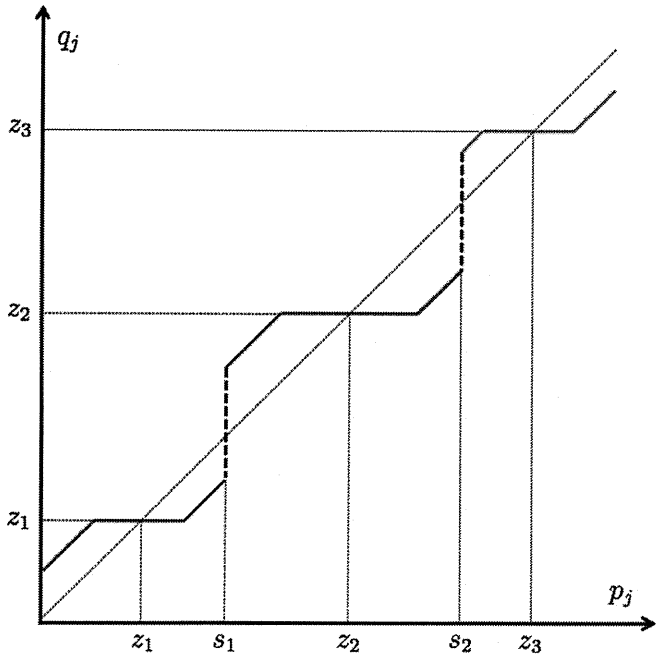

Figure 2. The multi-thresholding function in equation (21) with $L = 3$.

can be found through the following simple soft-thresholding function:

$$x^* = \begin{cases} a + \beta/\alpha & (a < b - \beta/\alpha) \\ b & (b - \beta/\alpha \leqslant a \leqslant b + \beta/\alpha) \\ a - \beta/\alpha & (a > b + \beta/\alpha). \end{cases} \tag{20}$$

In the same way, it is direct to estimate a multi-thresholding function corresponding to the minimization of the objective function in equation (16). Therefore, the iterative reconstruction algorithm is implemented through the following simple procedure. First, we compute the term p_j in equation (15) which is the same as a single iteration of the Convex algorithm (Lange and Fessler 1995). Then, the minimization is implemented through the following multi-thresholding function:

$$q_j = \begin{cases} p_j + 1/(2c_{j,l}) & (s_{l-1} < p_j < z^-_{j,l}) \\ z_l & (\max(z^-_{j,l}, s_{l-1}) \leqslant p_j \leqslant \min(z^+_{j,l}, s_l)) \\ p_j - 1/(2c_{j,l}) & (z^+_{j,l} < p_j \leqslant s_l) \end{cases}, \quad (l = 1, \ldots, L). \tag{21}$$

with $z^+_{j,l} = z_l + 1/(2c_{j,l})$, $z^-_{j,l} = z_l - 1/(2c_{j,l})$, $s_l = (\omega_l z_l + \omega_{l+1} z_{l+1})/(\omega_l + \omega_{l+1})$, $s_0 = -\infty$ and $s_L = \infty$.

This multi-thresholding function can be expressed as a combination of multiple successive soft-thresholding functions; each is implemented around a single value of the *a priori* known intensity values z_l, $l = 1, \ldots, L$. The practical interpretation of this thresholding operation is as follows. If the computed pixel value p_j is closed to the intensity value z_l (i.e. located inside the thresholding window controlled by the parameter ω_l), the pixel value is trimmed to z_l. Otherwise, the pixel value p_j is shifted *softly* toward the closest value of z_l. An illustration of the multi-thresholding functions is in figure 2.

In MAP reconstruction algorithms, the hyper-parameter β in equation (6) is known as the regularization parameter which handles the strength of the prior term. In the iMAP algorithm, β controls the size of the thresholding window in the multi-thresholding function in (21). Obviously, the value of β should be carefully selected. On the one hand, if β is assigned to a rather large value, some low-frequency details in the reconstructed image will be lost due to the strong thresholding. On the other hand, if β is relatively small, the merit of thresholding is weak and the proposed method behaves similar to the conventional reconstruction algorithm. We propose to use a dynamic value for this parameter by starting with a relatively large value and then gradually decrease it according to the following rule:

$$\lim_{k\to\infty} \beta_k = \delta \qquad \text{and} \qquad \sum_{k=0}^{\infty} \beta_k = \infty, \tag{22}$$

where δ is a small value empirically defined to represent the noise magnitude and equals to zero for noise-free data. In the experimental studies presented in this paper, we have used the ordered subset version of the proposed algorithm (OS-iMAP) to speed up the reconstruction, and the under-relaxation parameter is implemented using the following simple rule:

$$\beta_k = (k_{\max} + 1)\beta/(k + 1), \tag{23}$$

where $k_{\max}$ is the number of iterations used in the reconstruction. The use of this dynamic hyper-parameter is useful to speed up the convergence in the practical implementation. This approach is based on the observation that, in the early iterations, a strong thresholding is required to remove acute streak artifacts, and a weak thresholding is preferred later to retrieve missing small-size and low-contrast image details. Moreover, it is known that the use of the under-relaxation parameter improves the convergence properties of ordered subset reconstruction by removing the limit cycle behavior (Kole 2005).

The proposed iMAP algorithm has various advantages. First, the penalty function for intensity prior in equation (8) can be easily embedded in several famous transmission SR algorithms, for example, the EM algorithm (Lange and Carson 1984), gradient algorithm (Lange *et al* 1987) and its ordered subset version (Beekman and Kamphuis 2001). Second, the computation cost is almost same as the original method since the cost of the multi-thresholding step can be ignored relative to the computation of a single iteration of the original reconstruction algorithm. Third, the required intensity prior, as we will present in the next section, can be easily estimated with high accuracy in many imaging situations.

3.3. Estimation of intensity prior

In the iMAP algorithm presented above, we assume that a set of intensity values z is *a priori* known. In this section, we discuss possible approaches to compute the intensity prior.

3.3.1. Application-based estimation. In many x-ray CT applications, the anatomical structure as well as the attenuation coefficient of the target object can be estimated with high accuracy. The knowledge of the tube current energy and the exposure time used in the imaging equipment can provide an accurate limited range for the expected intensity values corresponding to the anatomy of the scanned object. For example, the standard intensity values, in Hounsfield units (HU), expected from the average radiation dose used in clinical CT scanners are shown in table 1 (Ohnesorge *et al* 2006). These values can be simply used as intensity prior in several CT imaging applications with weighting values ω that approximately represent the power of each intensity value.

Table 1. Standard attenuation values of body structures and other objects, measured in Hounsfield units (HU).

Anatomical structure	HU range
Air	−1000
Lung	−900 : −800
Fatty tissue	−100 : −50
Water	0
Blood	30 : 50
Muscles	30 : 80
Contrast enhanced blood	200 : 500
Calcification	130 : 500
Bone	500 : 1500
Metal	>1000

3.3.2. Image-based estimation. In some CT applications, such as IGRT, the patient is subject to multiple scans during a short time of treatment, which significantly increase the patient dose to a risky level. A possible alternative imaging protocol that minimizes the dose and also reduces the scan time can be as follows. First, the patient is imaged with a normal dose for a single time. The reconstructed image is used to estimate the intensity values that represent different regions of interest. The later periodic scans are then implemented through a low-dose or small views scan, which can be employed using intensity prior with the proposed method. Furthermore, it is possible to estimate the intensity values from a segmented image obtained from an earlier scan of the same patient or another patient. Moreover, in multi-slice CT imaging, the patient dose can be modulated by using a hybrid scan, which alternates the conventional scan in a single rotation and the low-dose scan in a few later ones. Intensity values obtained from slices reconstructed from normal dose data can be used for the reconstruction of the neighbor slices using data acquired from low-dose scans.

3.3.3. Data-based estimation.. If the *a priori* information about the internal anatomy of the scanned object is unknown, the intensity values can be estimated directly from the projection data through a clustering of image estimate. As shown later in the experimental studies, it is possible to estimate intensity values during the image reconstruction.

4. Experimental results

In this section, the proposed method is evaluated. The experiments are implemented using a simulated phantom and real data obtained from different x-ray CT imaging applications.

4.1. Assessment of image quality

Throughout the experimental data presented here, the image quality is measured using several methods. Along with each reconstruction result, the corresponding true object in simulated data or the FBP reconstruction from complete projection data is illustrated for visual evaluation. We also calculate the root mean square error (RMSE) for image quality evaluation:

$$\mathrm{RMSE}(\mu) = \sqrt{\sum_{j=1}^{n}(\mu_j - \bar{\mu}_j)^2 \Big/ \sum_{j=1}^{n}\bar{\mu}_j}, \tag{24}$$

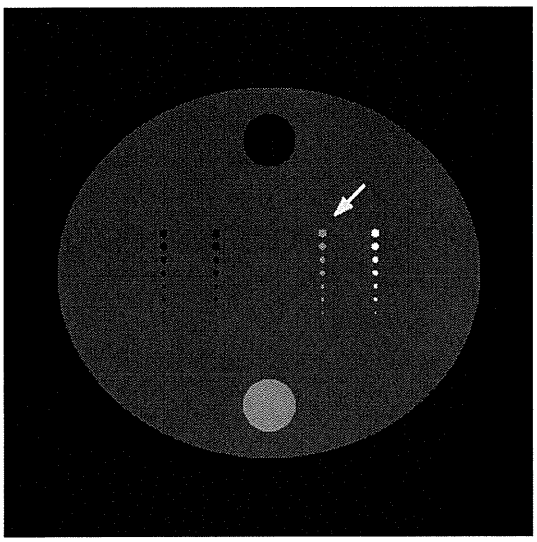

Figure 3. Digital phantom used in the simulation studies. The arrow is pointing to the column of seven resolution inserts used to compute the image contrast.

where $\bar{\mu}$ represents the true object or the FBP image reconstructed from complete data. We also measure the contrast of the reconstructed image using the following formula:

$$\text{contrast}(\mu) = \frac{|\mu_s - \mu_b|}{\mu_s + \mu_b}, \tag{25}$$

where μ_s and μ_b are the average intensity values of selected resolution insert pixels and background pixels, respectively.

4.2. Simulation studies

In the first simulation, we have used a digital phantom shown in figure 3. The phantom size is 100 mm consisting of a uniform background with resolution inserts of different size and contrast. The size of the inserts is ranged from 0.4 to 1.6 mm arranged in four columns each of seven inserts. Two additional inserts of 10 mm are also added to the phantom. The parameters of this phantom are shown in table 2. The image grid was set to 500 × 500 pixels, and the noise-free projection data were measured using a 500 bin detector over 180° with parallel-beam geometry and simple line-length model. The projection data were measured using 20, 10 and 7 projection views and the image reconstruction was implemented using FBP, OS-Convex, ART-TV (Sidky *et al* 2006) and OS-iMAP methods. The image reconstruction using the ART-TV method was implemented through a data enforcement step using the well-known ART algorithm followed by a TV-minimization step in an alternating manner. The parameters of the ART-TV method were optimized to obtain the best image on the RMSE scale. For iterative methods, the iteration number was unified to 100 iterations with an initial uniform image computed from projection data. The number of subsets used for the OS-Convex and OS-iMAP methods was set to 5, 5 and 7 subsets for reconstruction from 20, 10 and 7 view angles, respectively.

The intensity prior for the OS-iMAP method was selected to be the intensity values corresponding to air (region outside the object) and the uniform background of the phantom.

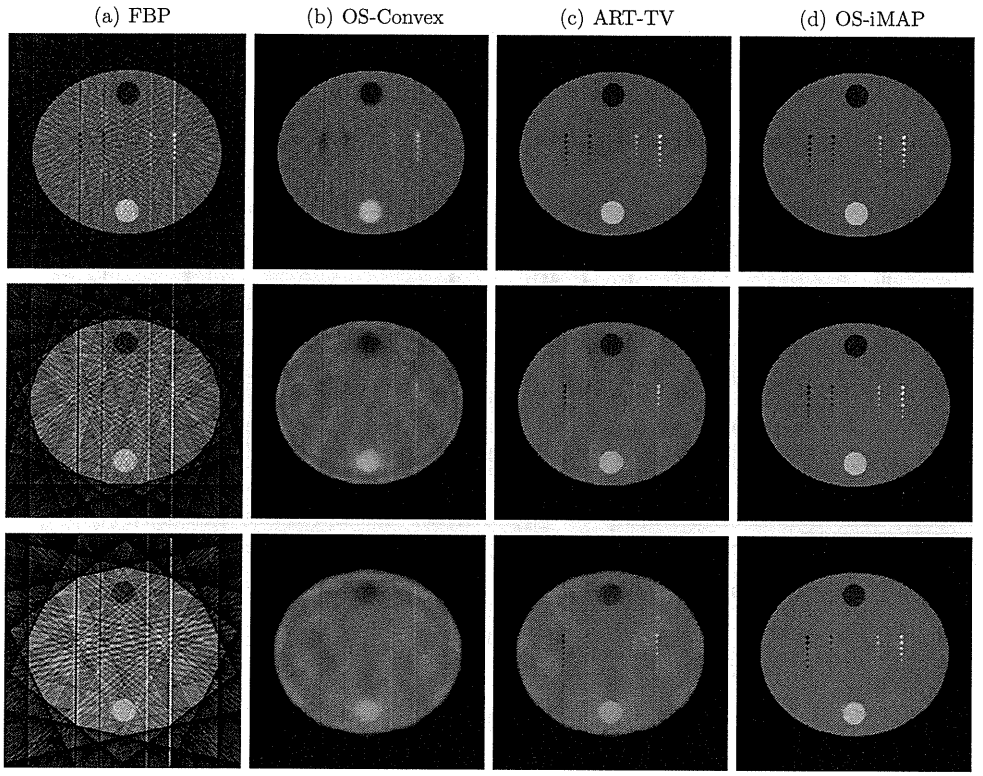

Figure 4. Images reconstructed using (a) standard FBP, (b) OS-Convex, (c) ART-TV and (d) OS-iMAP methods from 20, 10 and 7 projections (from top to bottom).

Table 2. Parameters of a digital phantom shown in figure 3. Objects from numbers 4–10 are repeated with $a = (-0.4, -0.2, 0.2, 0.4)$ and $b = (0.0, 0.5, 1.5, 2.0)$, respectively.

Index	Center coordinates	Major axis	Minor axis	Density (cm^{-1})
1	(0.0, 0.0)	0.8	0.7	1.0
2	(0.0, 0.5)	0.1	0.1	0.5
3	(0.0, −0.5)	0.1	0.1	1.5
4	(a, −0.15)	0.016	0.016	b
5	(a, −0.10)	0.014	0.014	b
6	(a, −0.05)	0.012	0.012	b
7	(a, 0.00)	0.010	0.010	b
8	(a, 0.05)	0.008	0.008	b
9	(a, 0.10)	0.006	0.006	b
10	(a, 0.15)	0.004	0.004	b

We assumed that the inserts are unknown structures. This assumption would probably fit with many diagnostic CT applications, where the intensity value of a uniform background is known while lesions are commonly unknown. The reconstruction was implemented with $L = 2$, $\beta = 0.008$, $z = (0.0, 1.0)$ cm^{-1} and $\omega = (0.01, 0.06)$. From only seven projections, the detectability of the inserts is significantly improved by using the proposed method. This can be confirmed by the visibility of the small-size inserts shown in figure 4 and the corresponding